Appl Phys B (2012) 107:1007–1017
DOI 10.1007/s00340-012-4905-0

Applied Physics B
Lasers and Optics

Model calculation of amplitudes for FT-ICR ion detection in a cylindrical Penning trap

M. Kretzschmar

Received: 30 April 2011 / Revised version: 7 September 2011 / Published online: 7 February 2012

Abstract A Green's function strategy first proposed by Grosshans et al. is used to calculate the electric charges induced by trapped ions on the 4-fold or 8-fold segmented ring electrode of a cylindrical Penning trap. The ions are assumed to move in the central region of the trap where the harmonic approximation holds. The electric charges induced on each detection segment of the ring electrode are obtained in the form of a triple Fourier series with coefficients that describe the contribution of each frequency combination $m_+\nu_+ + m_-\nu_- + m_z\nu_z$ as a function of R_+, R_-, Z, where ν_+, ν_-, ν_z are the characteristic frequencies and R_+, R_-, Z the corresponding amplitudes of the ion motion. The sideband structure is analyzed and the origin of the sidebands is tracked. Finally, single-electrode, differential, and additive detection are discussed.

1 Introduction

The Fourier transform ion cyclotron resonance (FT-ICR) method was first demonstrated in 1974 by Comisarow and Marshall [1] as a technique for the mass measurement of trapped ions. An account of the early history of the method is found in [2], and an introductory 'primer' in [3]. Recent developments have been extensively reviewed by Marshall [4] and by Marshall and Hendrickso [5]. The method is based on the measurement of electric image currents that are induced by the orbiting ions in the conducting surfaces of the trap electrodes. Contrary to time-of-flight methods [6], ion detection by the FT-ICR method is non-destructive and therefore of great interest for many experimental purposes. Whereas in past years mostly the collective FT-ICR signals of ion ensembles have been investigated [7], more recently interest has focussed also on the non-destructive detection by FT-ICR of single ions in radioactive beams [8–10].

The interpretation of the observed FT-ICR signals requires a sufficient theoretical background. A complete dynamical calculation is extremely complicated; however, model calculations based on reasonable physical assumptions may prove to be very helpful and provide insight into the structure of the observed FT-ICR signals. There is a choice between numerical and analytical approaches. While the former ones are very useful for practical laboratory work, the latter ones, although possibly less general, provide insights into the working of the theoretical machinery. A very general numerical model based on the reciprocity principle and image charge calculation within the SIMION modeling environment has been published by Hendrickson et al. [11]. It provides accurate numerical data for Fourier amplitudes in a wide class of trap geometries. Analytical approaches are possible only for a more limited class of problems because they require tools, such as explicit Green's functions, that are available only for a few specific trap geometries. On the other hand, where they are feasible they can provide general insights and rules, how Fourier amplitudes scale with the motional parameters of the ions, or how certain sidebands come about.

A general strategy for analytical investigations was outlined by Grosshans et al. [12]. For a kinematical prediction of FT-ICR signals they proposed a three-step procedure: (a) the charge induced by an ion on each of the detection electrodes must be calculated as a function of the ion position. This can be done by standard Green's function techniques, provided the Green's function with Dirichlet boundary conditions on the surface of the trap volume is known.

M. Kretzschmar (✉)
Institut für Physik, Johannes Gutenberg-Universität, 55099 Mainz, Germany
e-mail: martin.kretzschmar@uni-mainz.de

(b) From a known or assumed ion trajectory, the time dependence of the charge induced on the detector electrodes can then be found. (c) For a given geometrical arrangement of electrically interconnected detection electrodes, the expected FT-ICR signal must be derived.

The present paper follows this general scheme. We start by recalling some well-known facts about the calculation of the surface charge density induced by a point charge located at a fixed point inside the trap volume, using the Green's function of the Laplace equation with Dirichlet boundary conditions on the trap surface. We study a cylindrical Penning trap with a central ring electrode that is divided into four or eight segments serving as charge detectors or excitation electrodes for the purpose of FT-ICR measurements.

The ion motion is modeled as a motion in an ideal Penning trap, characterized by a modified cyclotron frequency $\omega_+ = 2\pi\nu_+$, a magnetron frequency $\omega_- = 2\pi\nu_-$, and an axial frequency $\omega_z = 2\pi\nu_z$, as well as the corresponding phases χ_+, χ_-, and χ_z and amplitudes R_+ (cyclotron radius), R_- (magnetron radius), and Z. This assumption is certainly valid as long as the ion orbits remain sufficiently close to the trap center in the region where the harmonic approximation holds. Beyond that region, corrections due to anharmonic potential terms must be taken into account.

This model calculation yields for the electric charges $\mathcal{Q}_i(t)$ induced on each of the four detection segments of the ring electrode ($i = 1, \ldots, 4$) expansions in a triple Fourier series with respect to the fundamental frequencies ω_+, ω_-, ω_z of the orbiting ion,

$$Q_i(t) = -q \sum_{m_+,m_-,m_z} W^{(i)}_{m_+,m_-,m_z}(R_+, R_-, Z) \times \cos\bigl(m_+(\omega_+ t + \chi_+) + m_-(\omega_- t + \chi_-) + m_z(\omega_z t + \chi_z)\bigr). \quad (1)$$

We find explicit expressions for the Fourier coefficients $W^{(i)}_{m_+,m_-,m_z}$ as functions of the radii R_+ and R_- and the axial amplitude Z. They indicate the strength of the FT-ICR signal expected at the frequency $m_+\omega_+ + m_-\omega_- + m_z\omega_z$ for the specified values of R_+, R_-, Z. The Fourier coefficients also contain information about the geometry of the specific cylindrical Penning trap. The signal for the modified cyclotron frequency ω_+ is discussed in greater detail together with its axial and magnetron sidebands.

2 Cylindrical Penning traps

This study assumes a cylindrical Penning trap of length L and radius a. A schematic view is shown in Fig. 1. The trap is assumed to be perfectly aligned with the homogeneous magnetic field; the trap axis is chosen as the z-axis of a coordinate system. The trap consists of two circular disks of radius a at the axial positions $z = 0$ and $z = L$,

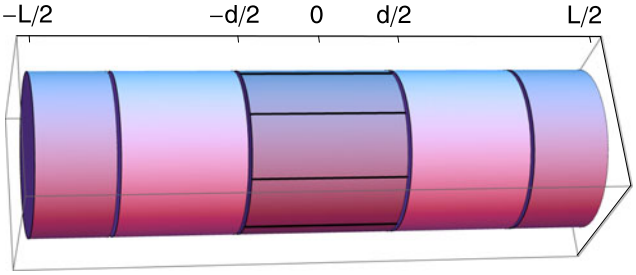

Fig. 1 Schematic view of a cylindrical Penning trap. The axial coordinate is $\zeta = z - L/2$. The central segmented ring electrode of length d serves for excitation and detection

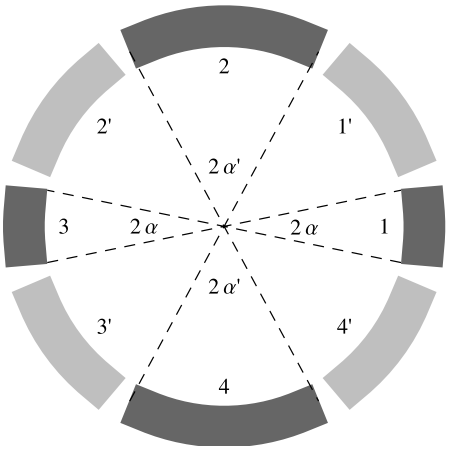

Fig. 2 Cut through an 8-fold segmented ring electrode. *Dark shaded segments* are detection electrodes $\mathcal{S}_i$ (opening angles 2α and $2\alpha'$, respectively), *lighter shaded segments* are excitation electrodes $\mathcal{S}'_i$

respectively, forming the end caps, and a number of cylindrical rings of radius a, forming the cylindrical main body of the trap, which extends over the interval $0 \le z \le L$ or, with $\zeta = z - L/2$, over $-L/2 \le \zeta \le L/2$. All components are assumed to be perfect electrical conductors. The central ring of length d, at the axial position $-d/2 \le \zeta \le +d/2$, is of special interest, because it is 4-fold or 8-fold segmented, the segments serving as excitation and detection electrodes. The trap center is located in the plane $z = L/2$ or $\zeta = 0$. A cut through the central ring electrode, perpendicular to the z-axis, is shown in Fig. 2.

Let us first define four detection segments $\mathcal{S}_i$, each defined by a given range of the azimuthal angle φ (angles are counted counterclockwise starting at the x-axis),

$$\mathcal{S}_i: \quad \alpha_{i,0} < \varphi < \alpha_{i,1} \quad (i = 1, 2, 3, 4), \quad (2)$$

with

$$\alpha_{1,0} = -\alpha, \qquad \alpha_{1,1} = \alpha, \quad (3)$$

$$\alpha_{2,0} = \pi/2 - \alpha', \qquad \alpha_{2,1} = \pi/2 + \alpha', \quad (4)$$

$$\alpha_{3,0} = \pi - \alpha, \qquad \alpha_{3,1} = \pi + \alpha, \quad (5)$$

$$\alpha_{4,0} = 3\pi/2 - \alpha', \qquad \alpha_{4,1} = 3\pi/2 + \alpha'. \quad (6)$$

By this definition, opposite segments are supposed to have the same opening angle, 2α in the case of $\mathcal{S}_1$ and $\mathcal{S}_3$, analogously $2\alpha'$ in the case of $\mathcal{S}_2$ and $\mathcal{S}_4$.

If $\alpha + \alpha' = \pi/2$, the four 'detection' segments $\mathcal{S}_i$ make up the complete ring electrode, which is then 4-fold segmented. However, if $\alpha + \alpha' < \pi/2$, there is room also for four 'excitation' electrodes $\mathcal{S}'_i$,

$$\mathcal{S}'_i: \quad \alpha_{i,1} < \varphi < \alpha_{i+1,0} \quad (\alpha_{4+1,0} = \alpha_{1,0}), \tag{7}$$

so that the ring electrode is now 8-fold segmented. For the following calculations, only the 'detection' segments shall be of interest.

Recent examples of cylindrical Penning traps with FT-ICR detection systems are the TRIGA trap at the University of Mainz [9], SHIPTRAP at GSI Darmstadt [10], and the KATRIN trap at Forschungszentrum Karlsruhe [13].

Many cylindrical traps used in actual experiments are open, i.e. there are no metallic surfaces at the ends to close the volume, the confining axial electric field being introduced via end rings at positive potential. Strictly speaking, the Green's function used in this paper would have to be modified for the open geometry. However, open cylindrical traps in actual use generally have large aspect ratios $r = L/2a$ in the range $r \approx 3$ or even larger. It has been shown by Grosshans et al. (see Fig. 8 in [12]), in agreement with our own calculations, that for aspect ratios $r \geq 2$ the difference between the open and the closed geometries becomes negligible. This argument applies even more when the detection segments, as is assumed in this paper, are part of the central ring electrode.

3 Surface charge density induced by a charge at a fixed position

3.1 General aspects

Consider a volume $\mathcal{V}$ enclosed by a grounded conducting surface Σ. The calculation of the surface charge density σ induced on Σ by a point charge q located at some point $\mathbf{x}_0$ in the interior of $\mathcal{V}$ is a well-known problem in electrostatics [14]. On account of Gauss's law, the total charge induced on Σ must equal $-q$; the induced charge density σ is, however, non-uniformly distributed, depending on the shape of the surface Σ and the location of q. The problem can be solved in a very general way by constructing the Green's function with Dirichlet boundary conditions on the surface Σ. These boundary conditions require $G_\mathrm{D}(\mathbf{x}; \mathbf{x}') = 0$ for $\mathbf{x} \in \Sigma$ and for $\mathbf{x}' \in \Sigma$. When G_D is known, the electric potential which is generated inside $\mathcal{V}$ by the charge q at $\mathbf{x}_0$ is given by

$$\Phi(\mathbf{x}, \mathbf{x}_0) = q G_\mathrm{D}(\mathbf{x}; \mathbf{x}_0). \tag{8}$$

The potential is vanishing on the surface Σ, and its derivative normal to the surface yields the surface charge on S, which is induced by the point charge q at $\mathbf{x}_0$:

$$\sigma(\mathbf{x}, \mathbf{x}_0) = \frac{q}{4\pi} \frac{\partial \Phi}{\partial n}\Big|_{\mathbf{x}\in S} = \frac{q}{4\pi} \frac{\partial}{\partial n} G_\mathrm{D}(\mathbf{x}; \mathbf{x}_0)\Big|_{\mathbf{x}\in S}. \tag{9}$$

Here the normal derivative $\partial/\partial n$ has been taken positive in the outward direction.

3.2 Implementation for a cylindrical geometry

The volume $\mathcal{V}$ is now specified to be a cylinder of radius a and length L. We define Cartesian (x, y, z) and cylindrical (ρ, φ, z) coordinates $x = \rho\cos\varphi$ and $y = \rho\sin\varphi$. The cylinder axis is the z-axis; the end faces are supposed to be located at $z = 0$ and $z = L$, the center of the cylinder is thus found at $z = L/2$. For this closed cylinder geometry, the Dirichlet Green's function is given in the literature (see [14], p. 134, Problem 3.21) as

$$\begin{aligned} &G_\mathrm{D}(\rho, z, \varphi; \rho', z', \varphi') \\ &\quad = \sum_{m=-\infty}^{+\infty} \mathrm{e}^{-\mathrm{i}m(\varphi-\varphi')} G_{|m|}(\rho, z; \rho', z'), \end{aligned} \tag{10}$$

with

$$\begin{aligned} &G_{|m|}(\rho, z; \rho', z') \\ &\quad = \frac{4}{L} \sum_{n=1}^{\infty} \sin\left(\frac{n\pi z}{L}\right) \sin\left(\frac{n\pi z'}{L}\right) \frac{\mathrm{I}_{|m|}(\frac{n\pi\rho_<}{L})}{\mathrm{I}_{|m|}(\frac{n\pi a}{L})} \\ &\qquad \times \left[\mathrm{I}_{|m|}\left(\frac{n\pi a}{L}\right)\mathrm{K}_{|m|}\left(\frac{n\pi\rho_>}{L}\right)\right. \\ &\qquad \left. - \mathrm{K}_{|m|}\left(\frac{n\pi a}{L}\right)\mathrm{I}_{|m|}\left(\frac{n\pi\rho_>}{L}\right)\right]. \end{aligned} \tag{11}$$

Here the functions $\mathrm{I}_{|m|}(x)$ and $\mathrm{K}_{|m|}(x)$ are modified Bessel functions with non-negative integer index. We also need the normal derivative of the Green's function on the cylinder surface $\rho = a$. This derivative can be simplified by making use of the Wronski determinant of the modified Bessel functions (see [14], p. 118). With

$$\begin{aligned} &\frac{\partial}{\partial\rho_>}\left[\mathrm{I}_{|m|}\left(\frac{n\pi a}{L}\right)\mathrm{K}_{|m|}\left(\frac{n\pi\rho_>}{L}\right)\right. \\ &\quad \left. - \mathrm{K}_{|m|}\left(\frac{n\pi a}{L}\right)\mathrm{I}_{|m|}\left(\frac{n\pi\rho_>}{L}\right)\right]\Big|_{\rho_>=a} = -\frac{1}{a}, \end{aligned} \tag{12}$$

we find

$$\begin{aligned} &\frac{\partial}{\partial\rho} G_{|m|}(\rho, z; \rho', z')\Big|_{\rho=a} \\ &\quad = -\frac{4}{aL} \sum_{n=1}^{\infty} \sin\left(\frac{n\pi z}{L}\right) \sin\left(\frac{n\pi z'}{L}\right) \frac{\mathrm{I}_{|m|}(\frac{n\pi\rho'}{L})}{\mathrm{I}_{|m|}(\frac{n\pi a}{L})}. \end{aligned} \tag{13}$$

In the next step, the coordinates are adapted to the calculation of the charges induced on the detection segments $\mathcal{S}_i$.

Let the primed coordinates signify the position of the ion: $\rho' = \rho_0, \varphi' = \varphi_0, z' = z_0$. The other set of coordinates refers to the cylinder surface, $\rho = a$, while φ and z vary over the cylinder surface.

3.3 Total surface charge induced on a detection segment $\mathcal{S}_i$

In this section, we consider an ion at the position $\mathbf{x}_0$ inside the trap and calculate the total electric charge $\mathcal{Q}_i(\mathbf{x}_0)$ induced on one of the detection segments $\mathcal{S}_i$. For this purpose, we integrate the charge density, (9), over the surface of the detection segment, using the Green's function (10)

$$\mathcal{Q}_i(\mathbf{x}_0) = \int_{\mathcal{S}_i} \mathrm{d}A\, \sigma(\mathbf{x}, \mathbf{x}_0) \quad (i = 1, \ldots, 4), \tag{14}$$

with the surface element $\mathrm{d}A = a\mathrm{d}\varphi\mathrm{d}z$.

The normal derivative in (9) does not involve the angular coordinate φ; therefore, the integral (14) can be factorized as

$$\mathcal{Q}_i(\mathbf{x}_0) = \sum_{m=0}^{\infty} \phi_{i,m}(\varphi_0)\, Q_m(\rho_0, z_0), \tag{15}$$

with

$$\phi_{i,m}(\varphi_0) = \int_{\alpha_{i0}}^{\alpha_{i1}} \mathrm{d}\varphi = \alpha_{i,1} - \alpha_{i,0} \quad \text{for } m = 0, \tag{16}$$

$$\phi_{i,m}(\varphi_0) = \int_{\alpha_{i0}}^{\alpha_{i1}} \mathrm{d}\varphi 2\cos\big(m(\varphi - \varphi_0)\big) \quad \text{for } m > 0, \tag{17}$$

and

$$Q_m(\rho_0, z_0) = \frac{qa}{4\pi} \int_{(L-d)/2}^{(L+d)/2} \mathrm{d}z \frac{\partial}{\partial n} G_m(a, z; \rho_0, z_0). \tag{18}$$

From here on, m will always be a non-negative integer, so that we can simplify the notation by writing $|m| = m$.

3.4 Angular integration

The angular integrals can be carried out immediately. For $m = 0$,

$$\phi_{1,0}(\varphi_0) = \phi_{3,0}(\varphi_0) = c_{1,0} = c_{3,0} = 2\alpha, \tag{19}$$

$$\phi_{2,0}(\varphi_0) = \phi_{4,0}(\varphi_0) = c_{3,0} = c_{4,0} = 2\alpha' \tag{20}$$

and, for $m > 0$,

$$\phi_{1,m}(\varphi_0) = c_{1,m} \cos m\varphi_0, \tag{21}$$

$$\phi_{2,m}(\varphi_0) = c_{2,m} \cos m(\varphi_0 - \pi/2), \tag{22}$$

$$\phi_{3,m}(\varphi_0) = c_{3,m} \cos m(\varphi_0 - \pi) = (-1)^m \phi_{1,m}(\varphi_0), \tag{23}$$

$$\begin{aligned}\phi_{4,m}(\varphi_0) &= c_{4,m} \cos m(\varphi_0 - 3\pi/2) \\ &= (-1)^m \phi_{2,m}(\varphi_0),\end{aligned} \tag{24}$$

with

$$c_{1,m} = c_{3,m} = \frac{4}{m} \sin(m\alpha), \tag{25}$$

$$c_{2,m} = c_{4,m} = \frac{4}{m} \sin\big(m\alpha'\big). \tag{26}$$

Hence, we can state

$$\phi_{1,m}(\varphi_0) + \phi_{3,m}(\varphi_0) \begin{cases} \neq 0 & \text{for even } m, \\ = 0 & \text{for odd } m, \end{cases} \tag{27}$$

$$\phi_{2,m}(\varphi_0) + \phi_{4,m}(\varphi_0) \begin{cases} \neq 0 & \text{for even } m, \\ = 0 & \text{for odd } m, \end{cases} \tag{28}$$

$$\phi_{1,m}(\varphi_0) - \phi_{3,m}(\varphi_0) \begin{cases} = 0 & \text{for even } m, \\ \neq 0 & \text{for odd } m, \end{cases} \tag{29}$$

$$\phi_{2,m}(\varphi_0) - \phi_{4,m}(\varphi_0) \begin{cases} = 0 & \text{for even } m, \\ \neq 0 & \text{for odd } m. \end{cases} \tag{30}$$

In Sect. 6, these results will be used to discuss the differential and additive detection of induced charges and currents.

3.5 Axial integration

As explained above, the charge detecting segments $\mathcal{S}_i$ are parts of the central cylindrical ring (see Fig. 1), having opening angles 2α and $2\alpha'$, respectively, and a total length d ($L/2 - d/2 \le z \le L/2 + d/2$). The integration over this length is independent of other operations and requires the integral $\int_{L/2-d/2}^{L/2+d/2} \mathrm{d}z \sin(n\pi z/L)$. It is easily seen that the integral vanishes for even n, while for odd values $n = 2j + 1$ we obtain

$$\begin{aligned}&\int_{L/2-d/2}^{L/2+d/2} \mathrm{d}z \sin\left(\frac{(2j+1)\pi z}{L}\right) \\ &\quad = \frac{(-1)^j 2L}{(2j+1)\pi} \sin\left(\frac{(2j+1)\pi d}{2L}\right).\end{aligned} \tag{31}$$

On the other hand, writing the axial position of the ion as $z_0 = L/2 + \zeta_0$, where ζ_0 denotes the axial deviation of the ion from the trap center, we find for odd $n = 2j + 1$

$$\sin\left(\frac{n\pi z_0}{L}\right) = (-1)^j \cos\left(\frac{(2j+1)\pi}{L}\zeta_0\right). \tag{32}$$

Inserting these results into (18), we obtain

$$\begin{aligned}Q_m(\rho_0, z_0) = -\frac{q}{4\pi}\frac{8}{\pi} \sum_{j=0}^{\infty} \frac{1}{2j+1} \sin\left(\frac{(2j+1)\pi}{2}\frac{d}{L}\right) \\ \times \cos\left(\frac{(2j+1)\pi}{L}\zeta_0\right) \frac{\mathrm{I}_m((2j+1)\pi\rho_0/L)}{\mathrm{I}_m((2j+1)\pi a/L)}.\end{aligned} \tag{33}$$

The total charge induced on segment $\mathcal{S}_i$ can now be calculated from (15),

$$\mathcal{Q}_i(\mathbf{x}_0) = -\frac{q}{4\pi}\frac{8}{\pi}\sum_{j=0}^{\infty}\frac{1}{2j+1}\sin\left(\frac{(2j+1)\pi}{2}\frac{d}{L}\right) \times\cos\left(\frac{(2j+1)\pi}{L}\zeta_0\right) \times\sum_{m=0}^{\infty}\phi_{i,m}(\varphi_0)\frac{\mathrm{I}_m((2j+1)\pi\rho_0/L)}{\mathrm{I}_m((2j+1)\pi a/L)}. \tag{34}$$

This is a rigorous result; no approximations have been introduced. Note that for a 4-fold segmented ring electrode ($\alpha+\alpha'=\pi/2$) with $d=L$ and $L\to\infty$ we obtain for a charge at the trap center $\sum_{i=1}^{4}\mathcal{Q}_i(0,0,L/2)=-q$, as expected.

4 Charges and currents induced by ions moving in a cylindrical Penning trap

The FT-ICR method is based on detecting electric charges on the trap electrodes that are induced by the orbiting trapped ions. The charges, or more precisely the electric currents due to the flow of these charges, are recorded as functions of time and are subsequently Fourier analyzed to reveal information on the ion motion.

So far, we have studied the surface charges induced on the detection segments $\mathcal{S}_i$ by an ion at a fixed position $\mathbf{x}_0$ inside the trap. Now we let the ion move along a trajectory $\mathbf{x}_0(t)$ inside the trap. As the position of the ion relative to the detector segments $\mathcal{S}_i$ changes, the induced charges will change correspondingly, and currents will flow between the detector segments and the ground. Since the mass of an ion of mass number $A\approx 50$ corresponds to 10^5 electron masses, we expect that the electrons in the metal surface reflect motions of the ion almost instantaneously and without noticeable back reaction on the ion, at least for short observation times.

4.1 Ion orbits

We assume that the ions perform a motion as is typical for Penning traps, with three fundamental frequencies $\nu_+ = \omega_+/(2\pi)$, $\nu_- = \omega_-/(2Pi)$, and $\nu_z = \omega_z/(2Pi)$, and with corresponding phase angles $\varphi_+(t)=\omega_+t+\chi_+$, $\varphi_-(t)=\omega_-t+\chi_-$, and $\varphi_z(t)=\omega_zt+\chi_z$ [15, 16]. The modified cyclotron frequency ν_+ is usually in the MHz range or above, while the axial frequency ν_z and the magnetron frequency ν_- are smaller by one or several orders of magnitude.

$$\begin{aligned} x(t) &= R_+\cos\varphi_+(t) + R_-\cos\varphi_-(t),\\ y(t) &= -R_+\sin\varphi_+(t) - R_-\sin\varphi_-(t),\\ z(t) &= L/2 + Z\cos\varphi_z(t). \end{aligned} \tag{35}$$

This assumption certainly holds near the center of the trap, where the harmonic approximation is valid. For larger orbits, one may try to apply corrections that take into account the anharmonic terms in the electrostatic potential and the corresponding shifts in the fundamental frequencies. Unfortunately, no analytic solutions are available; already the treatment of the lowest (quartic or octupolar) anharmonic term presents enormous difficulties [17, 18]. For this reason, (35) will be used in the subsequent calculations for lack of better alternatives.

The Cartesian relations (35) imply for the cylindrical coordinates ρ and φ

$$\rho(t) = \sqrt{R_+^2 + R_-^2 + 2R_+R_-\cos\big(\varphi_+(t)-\varphi_-(t)\big)}, \tag{36}$$

$$\varphi(t) = \arctan\left[-\frac{R_+\sin\varphi_+(t)+R_-\sin\varphi_-(t)}{R_+\cos\varphi_+(t)+R_-\cos\varphi_-(t)}\right]. \tag{37}$$

In complex notation, we can write

$$\begin{aligned} u(t) &= x(t)+\mathrm{i}y(t) = \rho(t)\mathrm{e}^{\mathrm{i}\varphi(t)}\\ &= R_+\exp\big[-\mathrm{i}\varphi_+(t)\big] + R_-\exp\big[-\mathrm{i}\varphi_-(t)\big]. \end{aligned} \tag{38}$$

4.2 Series expansions

The ion trajectory (35) will now be inserted into (34), so that the charges $\mathcal{Q}_i$ induced on the detection segments become time-dependent functions. In order to represent them as Fourier expansions, we use series expansions of $\cos x$ and of the modified Bessel function $\mathrm{I}_m(x)$ to extract and combine the time-dependent factors.

Beginning with the axial coordinate, we use (10.12.3) in [19] and find

$$\begin{aligned} &\cos\left(\frac{(2j+1)\pi Z}{L}\cos\varphi_z(t)\right)\\ &\quad= J_0\left((2j+1)\pi\frac{Z}{L}\right)\\ &\qquad+2\sum_{\ell=1}^{\infty}(-1)^{m_z}J_{2\ell}\left((2j+1)\pi\frac{Z}{L}\right)\cos\big(2\ell\varphi_z(t)\big), \end{aligned} \tag{39}$$

where the $J_n(x)$ are ordinary Bessel functions with integer index.

The radial coordinate occurs in the argument of the modified Bessel function I_m. The power series expansion of I_m yields

$$\mathrm{I}_m\left(\frac{(2j+1)\pi\rho(t)}{L}\right) = \sum_{k=0}^{\infty}\frac{((2j+1)\pi)^{m+2k}}{2^{m+2k}k!(m+k)!}\left(\frac{\rho(t)}{L}\right)^{m+2k}. \tag{40}$$

The time dependence due to the radial coordinate ρ is encoded in the powers $\rho(t)^{m+2k}$. Finally, the time dependence due to the angular coordinate enters via $\phi_{i,m}(t)$.

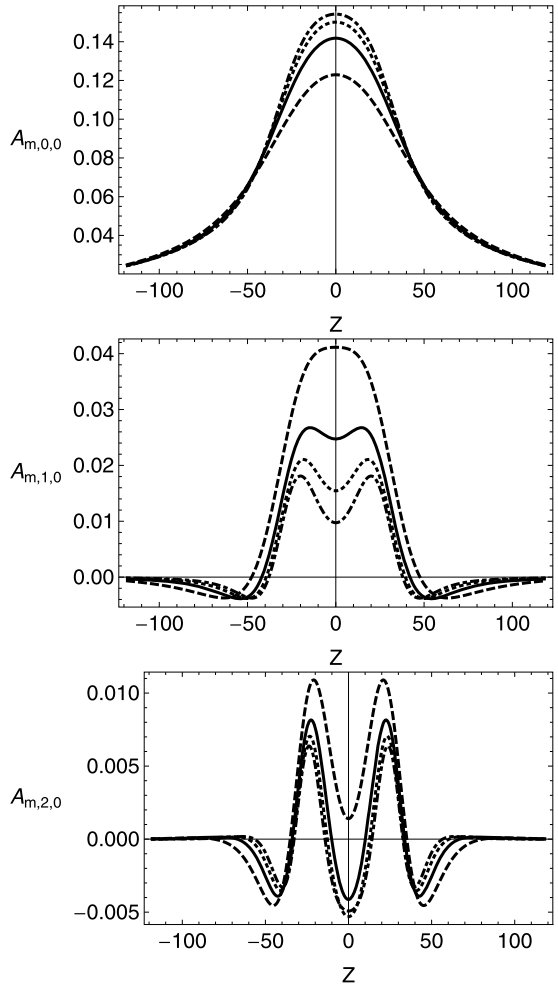

Fig. 3 Some coefficients $A_{m,k,0}(Z)$ calculated for the KATRIN trap. *Dashed line* $m = 0$, *solid line* $m = 1$, *dotted line* $m = 2$, *dot-dashed line* $m = 3$

Collecting these results, we obtain the series expansion

$$\begin{aligned}\mathcal{Q}_i(t) &= \sum_{m=0}^{\infty} \phi_{i,m}\big(\varphi(t)\big)\mathcal{Q}_m\big(\rho(t), z(t)\big) \\ &= -q \sum_{m=0}^{\infty}\sum_{k=0}^{\infty}\sum_{\ell=0}^{\infty} A_{m,k,\ell}(Z,a,L,d) \\ &\quad \times \cos\big(2\ell\varphi_z(t)\big)\phi_{i,m}\big(\varphi(t)\big)\left(\frac{\rho(t)}{a}\right)^{m+2k}, \end{aligned} \tag{41}$$

with coefficients $A_{m,k,\ell}$ that depend on the axial amplitude Z and on the geometry of the cylindrical trap, i.e. on the parameters a, d, and L.

$$\begin{aligned} A_{m,k,\ell}(Z) &= (2-\delta_{0,\ell})\frac{(-1)^\ell}{\pi^2}\frac{(\pi a/L)^{m+2k}}{k!(m+k)!} \\ &\quad \times \sum_{j=0}^{\infty} J_{2\ell}\left(\frac{(2j+1)\pi Z}{L}\right) \\ &\quad \times \sin\left(\frac{(2j+1)\pi d}{2L}\right) \\ &\quad \times \frac{(j+\frac{1}{2})^{m+2k-1}}{\mathrm{I}_m((2j+1)\pi a/L)}. \end{aligned} \tag{42}$$

The Kronecker symbol $\delta_{0,\ell}$ equals 1 for $\ell = 0$ and is zero otherwise. The remaining task is to represent the last line of (41) in the form of a Fourier series.

As an example, we display in Fig. 3 the Z-dependence of some coefficients $A_{m,k,l}(Z)$ calculated for the cylindrical trap at the KATRIN experiment [13]. The trap parameters are $a = 35.5$ mm, $L = 236$ mm, $d = 56$ mm, and $\alpha = 45°$. The coefficients depend strongly on the parameter d, the width of the detection segments.

4.3 The leading terms

At this point, we take a look at the leading terms in our series expansion; more precisely, we keep only the first term in the series expansion of the modified Bessel functions and disregard terms with $k \neq 0$. Equation (41) then reduces to

$$\begin{aligned}\mathcal{Q}_i(t) &= -q \sum_{m=0}^{\infty}\sum_{\ell=0}^{\infty} c_{i,m} A_{m,0,\ell}(Z)\cos\big(2\ell\varphi_z(t)\big) \\ &\quad \times \left(\frac{\rho(t)}{a}\right)^m \cos\big(m\big[\varphi(t) - (i-1)\pi/2\big]\big). \end{aligned} \tag{43}$$

We wish to write the induced charge in the form of a Fourier series. To this end, we raise (38) to the mth power to obtain

$$\begin{aligned}\rho^m(t)\mathrm{e}^{\mathrm{i}m\varphi(t)} &= \big(\rho(t)\mathrm{e}^{\mathrm{i}\varphi(t)}\big)^m \\ &= \big(R_+\exp\big[-\mathrm{i}\varphi_+(t)\big] + R_-\exp\big[-\mathrm{i}\varphi_-(t)\big]\big)^m \\ &= \sum_{j=0}^{m}\binom{m}{j} R_+^{m-j}R_-^j \\ &\quad \times \exp\big[-\mathrm{i}\big((m-j)\varphi_+(t) + j\varphi_-(t)\big)\big]. \end{aligned} \tag{44}$$

In view of (21)–(24), we generalize this result by performing a shift $\varphi(t) \to \varphi(t) - (i-1)\pi/2$ $(i = 1, \ldots, 4)$. Taking the real part of the generalized (44), we then obtain

$$\begin{aligned}&\rho^m(t)\cos\big[m\big(\varphi(t) - (i-1)\pi/2\big)\big] \\ &= \sum_{j=0}^{m}\binom{m}{j} R_+^{m-j}R_-^j \cos\big[(m-j)\varphi_+(t) + j\varphi_-(t) \\ &\quad + m(i-1)\pi/2\big]. \end{aligned} \tag{45}$$

Using (21)–(24) and inserting (45), we find

$$\begin{aligned}\mathcal{Q}_i(t) &= -q \sum_{m=0}^{\infty}\sum_{\ell=0}^{\infty} c_{i,m} A_{m,0,\ell}(Z) \sum_{j=0}^{m}\binom{m}{j} R_+^{m-j}R_-^j \\ &\quad \times \cos\big[2\ell\varphi_z(t)\big] \\ &\quad \times \cos\big[(m-j)\varphi_+(t) + j\varphi_-(t) + m(i-1)\pi/2\big]. \end{aligned} \tag{46}$$

We use the identity

$$\cos\varphi_1\cos\varphi_2 = (1/2)\big(\cos(\varphi_1+\varphi_2)+\cos(\varphi_1-\varphi_2)\big) \quad (47)$$

to combine the two cosine functions. The induced charge can then be written in the form of a Fourier series

$$\begin{aligned}\mathcal{Q}_i(t) = -q\sum_{m_+}\sum_{m_-}\sum_{m_z} W^{(i)}_{m_+,m_-,m_z}(R_+,R_-,Z)\\ \times\cos\big(m_+\varphi_+(t)+m_-\varphi_-(t)+m_z\varphi_z(t)\\ +\chi_{m_+,m_-,i}\big),\end{aligned} \quad (48)$$

with $\chi_{m_+,m_-,i} = (m_+ + m_-)(i-1)\pi/2$. The m_+ and m_- are non-negative integers, the m_z are positive or negative even integers. The Fourier amplitudes are

$$\begin{aligned}W^{(i)}_{m_+,m_-,m_z} = \frac{1}{2}(1+\delta_{0,\ell})c_{i,m}A_{m,0,\ell}(Z)\\ \times\binom{m_+ + m_-}{m_-}\left(\frac{R_+}{a}\right)^{m_+}\left(\frac{R_-}{a}\right)^{m_-},\end{aligned} \quad (49)$$

with $m = m_+ + m_-$ and $\ell = |m_z|/2$. Remember that the Z-dependence of $A_{m,0,\ell}$ originates from the Bessel function $J_{2\ell}$, so that $A_{m,0,\ell}(Z) \propto Z^{2\ell} = Z^{|m_z|}$.

We thus conclude that in leading order for all frequency combinations $m_+\omega_+ + m_-\omega_- + m_z\omega_z$, the Fourier amplitude is proportional to the monomial $R_+^{m_+}R_-^{m_-}Z^{|m_z|}$.

4.4 Higher corrections

The discussion must be completed by considering also the terms with $k \neq 0$. These terms are generally smaller than the leading terms by additional factors $(\rho(t)/a)^{2k}$. Equation (41) requires the calculation of $\rho(t)^{m+2k}\cos m\varphi(t)$. With (36), (44), and (47), one derives

$$\begin{aligned}\rho(t)^{m+2k}\cos m\varphi(t) = \sum_{m_+}\sum_{m_-} P^{m_+,m_-}_{m,k}(R_+,R_-)\\ \times\cos\big(m_+\varphi_+(t)+m_-\varphi_-(t)\big),\end{aligned} \quad (50)$$

where the $P^{m_+,m_-}_{m,k}(R_+,R_-)$ are uniquely determined homogeneous polynomials of degree $m+2k$ in the variables R_+ and R_-, with $m = m_+ + m_- \geq 0$. In the previous subsection, we encountered the special case

$$P^{m_+,m_-}_{m,0}(R_+,R_-) = \binom{m_+ + m_-}{m_-}R_+^{m_+}R_-^{m_-}. \quad (51)$$

Similarly as for (45), we must generalize (50) by performing a shift $\varphi(t) \to \varphi(t) - (i-1)\pi/2$ $(i = 1,\ldots,4)$ to take into account all four detection electrodes.

Instead of deriving a general formula for the polynomials $P^{m_+,m_-}_{m,k}(R_+,R_-)$, it is more convenient to illustrate their calculation by an example, say for $m = 3$ and $k = 2$. In that case, we have

$$\begin{aligned}\rho^3\cos 3\varphi\rho^4 &= \frac{1}{2}\big[\big(\rho e^{i\varphi}\big)^3 + \big(\rho e^{-i\varphi}\big)^3\big]\\ &\quad\times\big[R_+^2 + R_-^2 + 2R_+R_-\cos(\varphi_+-\varphi_-)\big]^2\\ &= \big[R_+^3\cos 3\varphi_+ + 3R_+^2R_-\cos(2\varphi_+ + \varphi_-)\\ &\quad + 3R_+R_-^2\cos(\varphi_+ + 2\varphi_-) + R_-^3\cos 3\varphi_-\big]\\ &\quad\times\big[R_+^4 + 4R_+^2R_-^2 + R_-^4 + 2R_+^2R_-^2\\ &\quad\times\cos(2\varphi_+ - 2\varphi_-)\\ &\quad + 4R_+R_-\big(R_+^2 + R_-^2\big)\cos(\varphi_+-\varphi_-)\big]\\ &= R_+^3\big(R_+^4 + 10R_+^2R_-^2 + 10R_-^4\big)\cos 3\varphi_+\\ &\quad + R_-^3\big(R_-^4 + 10R_+^2R_-^2 + 10R_+^4\big)\cos 3\varphi_-\\ &\quad + R_+^2R_-\big(5R_+^4 + 20R_+^2R_-^2 + 10R_-^4\big)\\ &\quad\times\cos(2\varphi_+ + \varphi_-)\\ &\quad + R_-^2R_+\big(5R_-^4 + 20R_+^2R_-^2 + 10R_+^4\big)\\ &\quad\times\cos(2\varphi_- + \varphi_+)\\ &\quad + R_+^4R_-\big(2R_+^2 + 5R_-^2\big)\cos(4\varphi_+ - \varphi_-)\\ &\quad + R_-^4R_+\big(2R_-^2 + 5R_+^2\big)\cos(4\varphi_- - \varphi_+)\\ &\quad + R_+^5R_-^2\cos(5\varphi_+ - 2\varphi_-) + R_-^5R_+^2\\ &\quad\times\cos(5\varphi_- - 2\varphi_+).\end{aligned} \quad (52)$$

This expression represents the desired double Fourier decomposition of $\rho^3\cos 3\varphi\rho^4$ with respect to the frequencies ω_+ and ω_-. The polynomials $P^{m_+,m_-}_{3,2}(R_+,R_-)$ can now be read off from this result as follows:

$$\begin{aligned}P^{3,0}_{3,2}(R_+,R_-) &= R_+^3\big(R_+^4 + 10R_+^2R_-^2 + 10R_-^4\big),\\ P^{0,3}_{3,2}(R_+,R_-) &= R_-^3\big(R_-^4 + 10R_+^2R_-^2 + 10R_+^4\big),\\ P^{2,1}_{3,2}(R_+,R_-) &= R_+^2R_-\big(5R_+^4 + 20R_+^2R_-^2 + 10R_-^4\big),\\ P^{1,2}_{3,2}(R_+,R_-) &= R_-^2R_+\big(5R_-^4 + 20R_+^2R_-^2 + 10R_+^4\big),\\ P^{4,-1}_{3,2}(R_+,R_-) &= R_+^4R_-\big(2R_+^2 + 5R_-^2\big),\\ P^{-1,4}_{3,2}(R_+,R_-) &= R_-^4R_+\big(2R_-^2 + 5R_+^2\big),\\ P^{5,-2}_{3,2}(R_+,R_-) &= R_+^5R_-^2,\\ P^{-2,5}_{3,2}(R_+,R_-) &= R_-^5R_+^2.\end{aligned}$$

Having explained the computational method, we display in Table 1 a number of low-degree polynomials for use in practical applications.

5 Detailed results

In this section, we classify and overview the expected detection signals. We first deal with the main signals, namely the multiples of the modified cyclotron frequency and the magnetron frequency. Thereafter magnetron and axial sidebands are discussed.

Table 1 The lowest polynomials $P_{m,k}^{m_+,m_-}(R_+, R_-)$

m	k	m_+	m_-	$P_{m,k}^{m_+,m_-}(R_+, R_-)$
0	0	0	0	1
0	1	0	0	$R_+^2 + R_-^2$
0	1	1	−1	$2R_+R_-$
0	2	0	0	$R_+^4 + 2R_+^2R_-^2 + R_-^4$
0	2	1	−1	$4R_+R_-(R_+^2 + R_-^2)$
0	2	2	−2	$2R_+^2R_-^2$
1	0	1	0	R_+
1	0	0	1	R_-
1	1	1	0	$R_+(R_+^2 + 2R_-^2)$
1	1	0	1	$R_-(R_-^2 + 2R_+^2)$
1	1	2	−1	$R_+^2R_-$
1	1	−1	2	$R_-^2R_+$
1	2	1	0	$R_+(R_+^4 + 6R_+^2R_-^2 + 3R_-^4)$
1	2	0	1	$R_-(R_-^4 + 6R_+^2R_-^2 + 3R_+^4)$
1	2	2	−1	$R_+^2R_-(R_+^2 + 3R_-^2)$
1	2	−1	2	$R_-^2R_+(R_-^2 + 3R_+^2)$
1	2	3	−2	$R_+^3R_-^2$
1	2	−2	3	$R_-^3R_+^2$
2	0	2	0	R_+^2
2	0	0	2	R_-^2
2	0	1	1	$2R_+R_-$
2	1	2	0	$R_+^2(R_+^2 + 3R_-^2)$
2	1	0	2	$R_-^2(R_-^2 + 3R_+^2)$
2	1	1	1	$3R_+R_-(R_+^2 + R_-^2)$
2	1	3	−1	$R_+^3R_-$
2	1	−1	3	$R_-^3R_+$

The general Fourier series for the detection signal at the detection segment $\mathcal{S}_i$ has been stated in (48). Including corrections with $k \neq 0$, the Fourier amplitude for the signal at the frequency $m_+\omega_+ + m_-\omega_- + m_z\omega_z$ can now be written as

$$W_{m_+,m_-,m_z}^{(i)}(R_+, R_-, Z) = \sum_{m=0}^{\infty}\sum_{k=0}^{\infty}\sum_{\ell=0}^{\infty}\frac{1}{2}(1+\delta_{0,\ell})\delta_{m,m_++m_-}\delta_{2\ell,m_z} \times c_{i,m}A_{m,k,\ell}(Z)\frac{1}{a^{m+2k}}P_{m,k}^{m_+,m_-}(R_+, R_-). \tag{53}$$

After evaluation of the Kronecker symbols in (53), the formal triple summation reduces to a single summation over k.

5.1 Signal at the modified cyclotron frequency ω_+: $m = m_+ = 1, m_- = m_z = 0$

This signal is the most important one for applications of FT-ICR spectrometry. In our theoretical model, its amplitude is given by

$$W_{1,0,0}^{(i)} = \frac{R_+}{a}\left(c_{i,1}A_{1,0,0}(Z) + \frac{c_{i,1}}{a^2}A_{1,1.0}(Z)\left(R_+^2 + 2R_-^2\right) + \frac{c_{i,1}}{a^4}A_{1,2,0}(Z)\left(R_+^4 + 6R_+^2R_-^2 + 3R_-^4\right) + \cdots\right). \tag{54}$$

For values $(R_\pm/a)^2 \ll 1$, the first term dominates and the signal rises linearly with R_+. For larger values of $R_\pm$, the correction terms for $k = 1, 2, \ldots$ must be taken into account.

5.2 Signal at the magnetron frequency ω_-: $m = m_- = 1$, $m_+ = m_z = 0$

This signal is less important for practical applications. The theoretical analysis is analogous to the preceding case, but with the roles of modified cyclotron and magnetron oscillators interchanged.

$$W_{0,1,0}^{(i)} = \frac{R_-}{a}\left(c_{i,1}A_{1,0,0}(Z) + \frac{c_{i,1}}{a^2}A_{1,1.0}(Z)\left(R_-^2 + 2R_+^2\right) + \frac{c_{i,1}}{a^4}A_{1,2,0}(Z)\left(R_-^4 + 6R_+^2R_-^2 + 3R_+^4\right) + \cdots\right). \tag{55}$$

5.3 Signal at higher harmonics of the modified cyclotron frequency $m_+\omega_+$: $m = m_+ \geq 1$, $m_- = m_z = 0$

Higher harmonics of ω_+ are observed and used in experiments. Equation (53) predicts the amplitude to be proportional to $(R_+/a)^{m_+}$:

$$W_{m_+,0,0}^{(i)} = \left(\frac{R_+}{a}\right)^{m_+}\left(c_{i,m_+}A_{m_+,0,0}(Z) + \frac{c_{i,m_+}}{a^2}A_{m_+,1,0}(Z) \times \left(R_+^2 + (m_+ + 1)R_-^2\right) + \cdots\right). \tag{56}$$

5.4 Signal at higher harmonics of the magnetron frequency $m_-\omega_-$: $m = m_- \geq 1$, $m_+ = m_z = 0$

The theoretical expectation is analogous to the previous case,

$$W_{0,m_-,0}^{(i)} = \left(\frac{R_-}{a}\right)^{m_-}\left(c_{i,m_-}A_{m_-,0,0}(Z) + \frac{c_{i,m_-}}{a^2}A_{m_-,1,0}(Z) \times \left(R_-^2 + (m_- + 1)R_+^2\right) + \cdots\right). \tag{57}$$

5.5 Signal at higher harmonics of the axial frequency $m_z\omega_z$: $|m_z| = 2\ell \neq 0$, $m = m_+ = m_- = 0$

Our model calculation assumes a cylindrical Penning trap that is perfectly aligned with the magnetic field and that has a geometry symmetric with respect to the substitution $\zeta \leftrightarrow -\zeta$, i.e. a reflection at the central plane of the trap ($\zeta = 0$ or $z = L/2$). As a consequence, we encounter only even functions of $\zeta = Z\cos(\omega_z t + \chi_z)$. There is no room in the model for odd functions of ζ and thus for odd multiples of ω_z. For even $|m_z| = 2\ell \neq 0$, we find from (53)

$$W^{(i)}_{0,0,m_z} = \sum_{k=0}^{\infty} \frac{1}{2} c_{i,0} A_{0,k,\ell}(Z) a^{-2k} P^{0,0}_{0,k}(R_+, R_-) = \frac{1}{2} c_{i,0} \left(A_{0,0,\ell}(Z) + A_{0,1,\ell}(Z) \frac{R_+^2 + R_-^2}{a^2} + \cdots \right). \tag{58}$$

5.6 Magnetron sidebands

Magnetron sidebands of the modified cyclotron frequency ω_+ are signals at frequencies $\omega_+ + m_-\omega_-$ differing from ω_+ by multiples of the magnetron frequency ω_-. For $m_- > 0$ we speak of a 'blue' sideband, for $m_- < 0$ of a 'red' sideband. The concept is extended in an obvious fashion to multiples of the modified cyclotron frequency $m_+\omega_+$. It is interesting to note that blue and red magnetron sidebands arise by different mechanisms and therefore are not expected to be symmetric. In fact, the blue sideband $m_+\omega_+ + m_-\omega_-$ ($m_- > 0$) originates in the expansion of $\rho^m(t)\cos[m\varphi(t)]$, (45) with $m = m_+ + m_-$. The Fourier amplitude for a blue magnetron sideband follows from (53) to be

$$W^{(i)}_{m_+,m_-,0} = \frac{R_+^{m_+} R_-^{m_-}}{a^{m_+ + m_-}} \left[c_{i,m} A_{m,0,0}(Z) \binom{m}{m_-} + c_{i,m} A_{m,1,0}(Z) \left[\binom{m+1}{m_-} \frac{R_+^2}{a^2} + \binom{m+1}{m_+} \frac{R_-^2}{a^2} \right] + \cdots \right]. \tag{59}$$

On the other hand, the red magnetron sidebands arise from higher terms in the expansion of the modified Bessel functions, (40),

$$\rho^{2k}(t) = \left(R_+^2 + R_-^2 + 2R_+R_-\cos\big(\varphi_+(t) - \varphi_-(t)\big)\right)^k = 2^k R_+^k R_-^k \cos\big[k\big(\varphi_+(t) - \varphi_-(t)\big)\big] + \cdots. \tag{60}$$

Consider for example the red magnetron sideband $m_+\omega_+ - k\omega_-$ ($k > 0$). Its leading term arises from

$$\big(\rho(t)\big)^{m_+ - k} \cos\big[(m_+ - k)\varphi(t)\big] \rho^{2k}(t) = 2^k R_+^{m_+} R_-^k \cos\big[(m_+ - k)\varphi_+(t)\big] \times \cos\big[k\big(\varphi_+(t) - \varphi_-(t)\big)\big] + \cdots. \tag{61}$$

Applying the identity (47) to the product of the cosines, the right-hand side supplies the leading term for the red sideband $m_+\omega_+ - k\omega_-$ and a correction term for the blue sideband $(m_+ - 2k)\omega_+ + k\omega_-$. Thus, the leading contribution for the red sideband $m_+\omega_+ - k\omega_-$ is found to be

$$W^{(i)}_{m_+,-k,0} = c_{i,m} A_{m,k,0}(Z) \frac{1}{2} \frac{R_+^{m_+} R_-^k}{a^{m_+ + k}} + \cdots, \tag{62}$$

with $m = m_+ - k$.

5.7 Axial sidebands

All signals at the multiples of the modified cyclotron frequency $m_+\omega_+$ and their magnetron sidebands $m_+\omega_+ + m_-\omega_-$ are accompanied by 'blue' and 'red' axial sidebands at frequencies $m_+\omega_+ + m_-\omega_- + 2\ell\omega_z$ and $m_+\omega_+ + m_-\omega_- - 2\ell\omega_z$ ($\ell = 1, 2, 3, \ldots$). This follows from (41) when we apply the identity (47) to the product $\cos(2\ell\varphi z)\cos(m_+\varphi_+ + m_-\varphi_-)$. It follows that the amplitudes at the blue axial sidebands must have the same magnitudes as at the corresponding red sidebands.

6 Detection schemes

In the preceding sections, we have calculated the electric charge $Q_i(t)$ induced on the single detection segment $\mathcal{S}_i$ by the moving ions. Measuring and Fourier analyzing the currents flowing between the ground and detection segment $\mathcal{S}_i$ represents the basic detection procedure. All results discussed above refer to this case (single-electrode detection).

Stronger signals are obtained by the use of two opposite detection electrodes, $\mathcal{S}_1$, $\mathcal{S}_3$ or $\mathcal{S}_2$, $\mathcal{S}_4$, either subtracting (differential or dipole detection) or adding (sum or quadrupole detection) the corresponding signals [20–23]. Here we wish to remark that on account of (27)–(30) the two detection schemes discriminate between $m = m_+ + m_-$ odd and even. Dipole detection selects odd m, we see Fourier signals at $\omega_\pm$, $3\omega_\pm$, $\omega_+ \pm 2\omega_-$, and so on, while quadrupole detection selects even m, we see Fourier signals at $2\omega_\pm$, $4\omega_\pm$, $\omega_+ \pm \omega_-$, $\omega_+ \pm 3\omega_-$, and so on.

Consider specifically the modified cyclotron frequency ω_+. In dipole detection, we expect to see the even magnetron sidebands $\omega_+ \pm 2k\omega_-$, while in quadrupole detection the odd sidebands $\omega_+ \pm (2k+1)\omega_-$ are seen.

For an overview of experimental work and numerical modeling relating to sidebands and various detection schemes, see Grosshans et al. [12] and Hendrickson et al. [11]. Our analytical results corroborate their findings.

7 Application to ion cyclotron resonance

In recent experimental work, Heck et al. [24] have investigated by the FT-ICR method the interconversion between

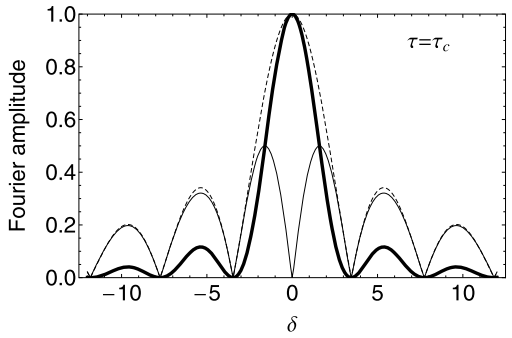

Fig. 4 Conversion line shape for quadrupole excitation with pulse duration $\tau = \tau_c$ (i.e. complete conversion at frequency $\nu_c = \nu_+ + \nu_-$). *Thick solid line*: conversion profile as measured with ToF-ICR mass spectrometry and predicted for FT-ICR mass spectrometry at frequency $2\nu_+$. *Thin solid line*: conversion profile predicted for FT-ICR mass spectrometry at frequency $\nu_c = \nu_+ + \nu_-$. *Dashed line*: conversion profile predicted for FT-ICR mass spectrometry at frequency ν_+

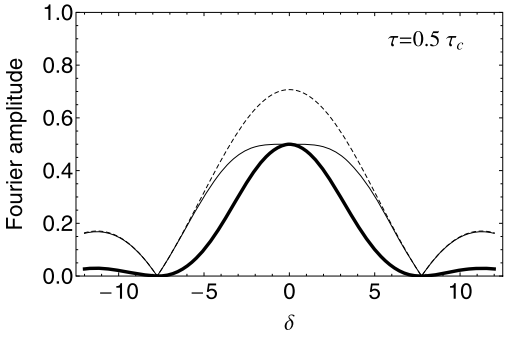

Fig. 5 Same as Fig. 4, but with pulse duration $\tau = 0.5\tau_c$

the magnetron and the cyclotron motional modes in a Penning trap due to a quadrupolar rf field with a frequency near the cyclotron frequency.[1] The height of the FT-ICR signal at the modified cyclotron frequency ν_+ was monitored while the frequency of the rf field was scanned over an interval about the true cyclotron frequency ν_c. According to the model calculation developed in this paper, this signal should be proportional to the cyclotron radius of the ions at the end of the rf pulse, $R_+(\tau;\delta)$, where δ denotes the detuning of the quadrupolar rf field (see (54)). For comparison, conversion profiles obtained by the time-of-flight ion-cyclotron-resonance (ToF-ICR) method are proportional to $n_+(\tau,\delta) = R_+^2(\tau;\delta)/R_-^2(0)$. Thus, FT-ICR profiles taken at frequency ν_+ must be squared for comparison with the ToF-ICR profiles. On the other hand, according to (56), FT-ICR profiles taken at frequency $2\nu_+$ should be proportional to $R_+^2(\tau;\delta)$ and thus proportional to the ToF-ICR profiles.

A very different conversion profile is obtained when data are taken at the true cyclotron frequency $\nu_c = \nu_+ + \nu_-$. The FT-ICR amplitude is now expected to be proportional to $R_+(\tau;\delta)R_-(\tau;\delta)$ according to (59). Starting with ions in pure magnetron motion, we expect complete conversion into cyclotron motion after a quadrupolar excitation of duration τ_c and with detuning $\delta = 0$. This means $R_-(\tau_c;\delta = 0) = 0$; thus, we expect a zero in the FT-ICR conversion profile at the resonance frequency ν_c.

This has been illustrated in Figs. 4 and 5, where we compare FT-ICR conversion profiles taken at the modified cyclotron frequency ν_+ (dashed line), at $2\nu_+$ (thick solid line), and at the true cyclotron frequency $\nu_c = \nu_+ + \nu_-$ (thin solid line). Figure 4 shows FT-ICR profiles after a pulse duration τ_c, when we expect complete conversion for $\delta = 0$. Figure 5 shows the expected FT-ICR profiles after a duration of the quadrupole excitation of only $0.5\ \tau_c$.

[1] For a more detailed theoretical discussion, see [24].

8 Conclusions

In this work, we have theoretically investigated the Fourier amplitudes relevant for FT-ICR ion detection in a cylindrical Penning trap with a 4-fold or 8-fold segmented ring electrode. Using a Green's function strategy proposed by Grosshans et al. [12], explicit expressions were obtained for the electric charge induced on the detection segments of the ring electrode. Ion orbits were assumed to remain sufficiently close to the trap center in a region where anharmonic potential terms do not yet play a significant role. The expression for the induced charge could then be written as a triple Fourier series

$$Q_i(t) = \sum W^{(i)}_{m_+,m_-,m_z}(R_+, R_-, Z) \times \cos\big[(m_+\omega_+ + m_-\omega_- + m_z\omega_z)t\big], \tag{63}$$

where m_+, m_-, m_z are integers $0, \pm1, \pm2, \ldots$, and where $R_\pm$ and Z are the cyclotron and magnetron radii and the axial amplitude, respectively. The coefficients $W_{m_+,m_-,m_z}(i)(R_+, R_-, Z)$ indicate the strength of the FT-ICR signal at the frequency combination $m_+\omega_+ + m_-\omega_- + m_z\omega_z$ and its dependence on R_+, R_-, and Z. The mathematical derivation shows that

$$W^{(i)}_{m_+,m_-,m_z}(R_+, R_-, Z) \propto (R_+/a)^{|m_+|}(R_-/a)^{|m_-|}(Z/L)^{|m_z|}. \tag{64}$$

The fact that $R_\pm/a < 1$ and $Z/L \ll 1$ establishes a hierarchy of detection frequencies, with the modified cyclotron frequency ω_+ and the magnetron frequency ω_- taking the leading positions. Higher harmonics as well as magnetron and axial sidebands of these frequencies were discussed. In all cases, analytic expressions for the magnitudes of the Fourier amplitudes were worked out. The theory provides insight into the different origins of 'blue' and 'red' magnetron sidebands, which give rise to an asymmetry, and into

why the blue sidebands may be expected to be more prominent than the red sidebands. Similarly, it is made clear why blue and red axial sidebands occur only at even multiples of the axial frequency and why corresponding blue and red axial sidebands must have amplitudes of equal magnitude. These results are in agreement with the findings of various experiments and numerical [11] and analytical studies [12].

References

1. M.B. Comisarow, A.G. Marshall, Chem. Phys. Lett. **25**, 282 (1974)
2. M.B. Comisarow, A.G. Marshall, J. Mass Spectrom. **31**, 581 (1996)
3. A.G. Marshall, C.L. Hendrickson, G.S. Jackson, Mass Spectrom. Rev. **17**, 1 (1998)
4. A.G. Marshall, Int. J. Mass Spectrom. **200**, 331 (2000)
5. A.G. Marshall, C.L. Hendrickson, Int. J. Mass Spectrom. **215**, 59 (2002)
6. G. Gräff, H. Kalinowsky, J. Traut, Z. Phys. A **297**, 35 (1980)
7. R.S. van Dyck Jr., F.L. Moore, D.L. Farnham, P.B. Schwinberg, Phys. Rev. A **40**, 6308 (1989)
8. K. Blaum, Phys. Rep. **425**, 1 (2006)
9. J. Ketelaer, K. Blaum, M. Block, K. Eberhardt, R. Ferrer, S. George, F. Herfurth, J. Ketter, Sz. Nagy, W. Nörtershäuser, J. Repp, L. Schweikhard, C. Smorra, S. Sturm, S. Stahl, Eur. Phys. J. A **42**, 311 (2008)
10. R. Ferrer, K. Blaum, M. Block, F. Herfurth, J. Ketelaer, Sz. Nagy, S. Schwarz, L. Schweikhard, C. Yazidjan, Eur. Phys. J. Spec. Top. **150**, 347 (2007)
11. C.L. Hendrickson, S.C. Beu, G.T. Blakney, A.G. Marshall, Int. J. Mass Spectrom. **283**, 100 (2009)
12. P.B. Grosshans, P.J. Shields, A.G. Marshall, J. Chem. Phys. **94**, 5341 (1991)
13. M. Ubieto-Diaz, D. Rodriguez, S. Lukic, Sz. Nagy, S. Stahl, K. Blaum, Int. J. Mass Spectrom. **288**, 1 (2009)
14. J.D. Jackson, *Classical Electrodynamics*, 2nd edn. (Wiley, New York, 1975)
15. L.S. Brown, G. Gabrielse, Rev. Mod. Phys. **58**, 233 (1986)
16. M. Kretzschmar, Eur. J. Phys. **12**, 240 (1991)
17. G.Zs.K. Horvath, J.-L. Hernandez-Pozos, K. Dholakia, J. Rink, D.M. Segal, R.C. Thompson, Phys. Rev. A **57**, 1944 (1998)
18. M. Lara, J.P. Salas, Chaos **14**, 763 (2004)
19. F.W.J. Olver, D.W. Lozier, R.F. Boisvert, C.W. Clark, *NIST Handbook of Mathematical Functions* (Cambridge University Press, Cambridge, 2010)
20. L. Schweikhard, M. Blundschling, R. Jertz, H.-J. Kluge, Rev. Sci. Instrum. **60**, 2631 (1989)
21. L. Schweikhard, M. Lindinger, H.-J. Kluge, Int. J. Mass Spectrom. Ion Process. **98**, 25 (1990)
22. L. Schweikhard, Rapid Commun. Mass Spectrom. **4**, 360 (1990)
23. L. Schweikhard, Int. J. Mass Spectrom. Ion Process. **107**, 281 (1991)
24. M. Heck, K. Blaum, R.B. Cakirli, M. Kretzschmar, G. Marx, D. Rodríguez, L. Schweikhard, S. Stahl, M. Ubieto-Díaz, Appl. Phys. B (2011). doi:10.1007/s00340-011-4865-9